LA-UR-19-22684 (Accepted Manuscript)

Reversible Electrochemical Phase Change in Monolayer to Bulk-like MoTe2 by Ionic Liquid Gating

Zakhidov, Dante
Rehn, Daniel Adam
Reed, Evan J
Salleo, Alberto

Provided by the author(s) and the Los Alamos National Laboratory (2020-03-03).

To be published in: ACS Nano

DOI to publisher's version: 10.1021/acsnano.9b07095

Permalink to record: http://permalink.lanl.gov/object/view?what=info:lanl-repo/lareport/LA-UR-19-22684

Disclaimer:
Los Alamos National Laboratory, an affirmative action/equal opportunity employer, is operated by Triad National Security, LLC for the National Nuclear Security Administration of U.S. Department of Energy under contract 89233218CNA000001. By approving this article, the publisher recognizes that the U.S. Government retains nonexclusive, royalty-free license to publish or reproduce the published form of this contribution, or to allow others to do so, for U.S. Government purposes. Los Alamos National Laboratory requests that the publisher identify this article as work performed under the auspices of the U.S. Department of Energy. Los Alamos National Laboratory strongly supports academic freedom and a researcher's right to publish; as an institution, however, the Laboratory does not endorse the viewpoint of a publication or guarantee its technical correctness.

ACSNANO

www.acsnano.org

ARTICLE

Reversible Electrochemical Phase Change in Monolayer to Bulk-like $MoTe_2$ by Ionic Liquid Gating

Dante Zakhidov, Daniel A. Rehn, Evan J. Reed, and Alberto Salleo*

Cite This: https://dx.doi.org/10.1021/acsnano.9b07095

Read Online

ACCESS | Metrics & More | Article Recommendations | Supporting Information

ABSTRACT: Transition-metal dichalcogenides (TMDs) exist in various crystal structures with semiconducting, semi-metallic, and metallic properties. The dynamic control of these phases is of immediate interest for next-generation electronics such as phase change memories. Of the binary Mo and W-based TMDs, $MoTe_2$ is attractive for electronic applications because it has the lowest energy difference (40 meV) between the semiconducting (2H) and semi-metallic (1T′) phases, allowing for $MoTe_2$ phase change by electrostatic doping. Here, we report phase change between the 2H and 1T′ polymorphs of $MoTe_2$ in thicknesses ranging from the monolayer to bulk-like case (73 nm) using an ionic liquid electrolyte at room temperature and in air. We find consistent evidence of a partially reversible 2H-1T′ transition using *in situ* Raman spectroscopy where the phase change occurs in the topmost layers of the $MoTe_2$ flake. We find a thickness-dependent transition voltage where higher voltages are necessary to drive the phase change for thicker flakes. We also show evidence of electrochemical activity during the gating process by observation of Te metal formation. This finding suggests the formation of Te vacancies which have been reported to lower the energy difference between the 2H and 1T′ phases, potentially aiding the phase change process. Our discovery that the phase change can be achieved on the surface layer of bulk-like materials reveals that this electrochemical mechanism does not require isolation of a single layer and the effect may be more broadly applicable than previously thought.

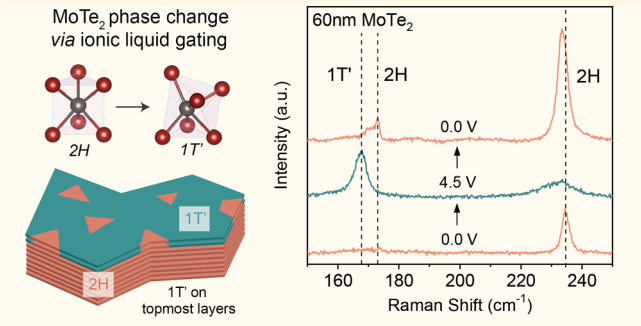

KEYWORDS: *phase change, transition-metal dichalcogenides, $MoTe_2$, ionic liquid gating, electrostatic, vacancies*

Since the discovery of graphene,[1] the field of two-dimensional (2D) materials has rapidly grown with the introduction of new classes of 2D materials such as buckled, single-element Xenes[2] (silicene, germanene, tellurene), transition-metal carbides and nitrides called MXenes[3,4] (Ti_3C_2, Ti_4N_3), and the transition-metal dichalcogenides[5,6] (MoS_2, WTe_2, $TaSe_2$). The study of these materials has been motivated by their attractive thermal, electronic, optical, and catalytic properties that can be tuned not only by size, composition, and functionalization but also more fundamentally altered by their crystal structure or phase. 2D materials often exhibit polymorphism, with crystal phases in a given material having vastly different electronic structures that allow for phenomena such as ferroelectricity, piezoelectricity, charge density waves, superconductivity, and their corresponding applications.[1−6] Particularly, the ability to switch between semiconducting and metallic phases in the transition-metal dichalcogenides (TMDs) is of immediate interest for next-generation electronics such as phase change electronic memories and other applications due to their unique properties, smaller device footprint, and potentially lower energetic switching costs.[7,8]

The majority of research on phase equilibria has focused on the group VI TMDs (MoX_2, WX_2) between the main polymorphs which are the trigonal-prismatic coordinated, semiconducting 2H phase; the octahedral coordinated, metallic 1T phase; and the distorted octahedral-coordinated, semi-metallic 1T′ phase (Figure 1a).[9] Phase control and phase change have been reported in group VI TMDs by means of alkali-metal intercalation,[10] alloying,[11,12] strain,[13,14] joule heating,[15] thermal treatment,[16,17] and electrostatic gating.[18] Out of those binary TMDs, $MoTe_2$ has the lowest energy difference between the semiconducting 2H and the semi-metallic 1T′ phase with the potential to further reduce the energy difference by alloying with

Received: September 6, 2019
Accepted: February 11, 2020
Published: February 11, 2020

Downloaded via LOS ALAMOS NATL LABORATORY on February 19, 2020 at 17:19:59 (UTC).
See https://pubs.acs.org/sharingguidelines for options on how to legitimately share published articles.

© XXXX American Chemical Society

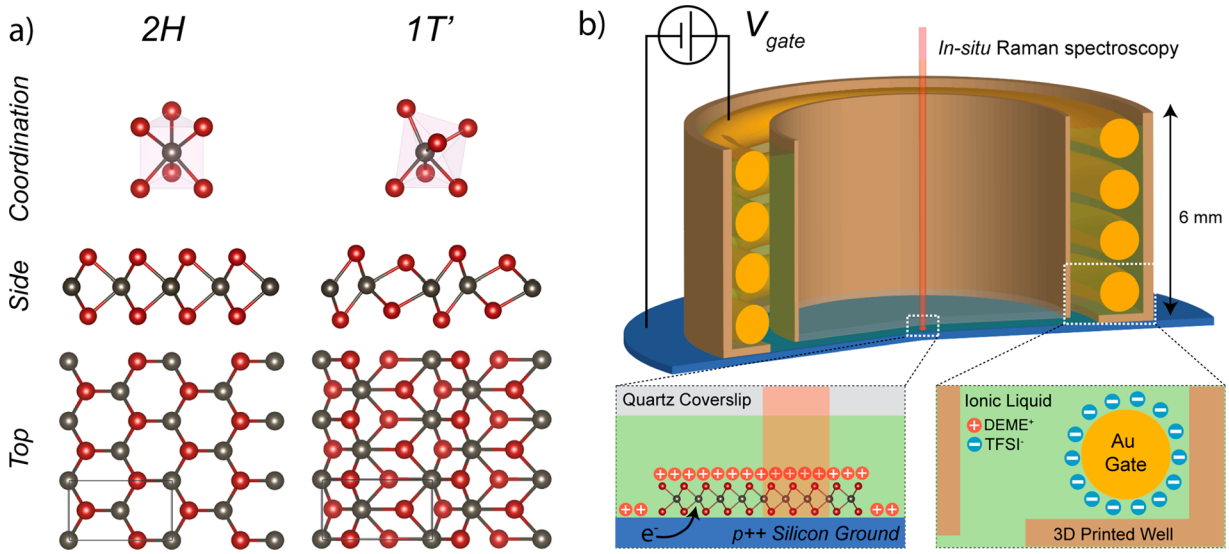

Figure 1. Crystalline phases of $MoTe_2$ and ionic liquid gating structure. (a) Crystal structure of 2H and 1T′ $MoTe_2$ phases. The gray atoms represent molybdenum, and the red atoms represent tellurium. The 2H phase is semiconducting with a trigonal prismatic coordination, and the 1T′ phase is semi-metallic with a distorted octahedral coordination. (b) Measurement cell and configuration used to manipulate the $MoTe_2$ phase during *in situ* Raman spectroscopy. The $MoTe_2$ is exfoliated onto a *p*++ silicon substrate which doubles as an electrode for charge carrier injection. A plastic 3D-printed well houses the gate and the DEME-TFSI ionic liquid. A gold wire is coiled within the measurement cell, and the length and corresponding surface area of the gold gate are chosen in such a way as to not limit the gating process. A thin quartz coverslip attached to an inner well is used to minimize the volume of ionic liquid along the Raman laser path.

W.[9,19] Furthermore, computational work on monolayer $MoTe_2$ showed that the low-energy difference between 2H and 1T′ makes the phase transition obtainable by charging *via* electrostatic gating.[20] Electrostatic phase change by means of field-induced charge doping remains the most attractive switching mechanism for device technologies because of its potential to be reversible, energy-efficient, and fast. The density functional theory (DFT) studies were first experimentally confirmed by Wang *et al.*, who showed reversible phase change in monolayer $MoTe_2$ using a gated ionic liquid at 220 K under vacuum.[18]

We extend the study by Wang *et al.* to demonstrate phase change in a range of thicknesses of $MoTe_2$, from the monolayer to bulk-like case (73 nm), using ionic-liquid gating with *N*,*N*-diethyl-*N*-(2-methoxyethyl)-*N*-methylammonium bis-(trifluoromethylsulfonyl)-imide (DEME-TFSI) at room temperature and in air. We find consistent evidence of a partially reversible 2H-1T′ transition using *in situ* Raman spectroscopy and demonstrate the appearance of two additional 1T′ Raman modes that are widely reported in pristine 1T′ but previously not reported in 1T′ $MoTe_2$ produced by phase change from the 2H phase. We empirically find that the transition voltage increases with thickness, suggesting that higher charge densities are necessary for thicker flakes. Ultimately, we demonstrate that our phase change is not only electrostatic but also electrochemically mediated by the creation of Te vacancies during the gating process. Te vacancies have been reported to lower the energy difference between the 2H and 1T′ phases[16,21−23] and likely decrease the doped charge density necessary to switch $MoTe_2$ flakes thicker than a monolayer. Additionally, polarization-resolved Raman measurements suggest that the 1T′ phase produced by our experimental conditions is polycrystalline, with domains forming heterogeneously along different 2H crystallographic directions. These results display $MoTe_2$ phase change in a variety of practical conditions, providing promise for $MoTe_2$ in phase change memories. They also suggest that controlled vacancy creation or flake thickness can be a valuable knob in tuning the transition voltage for phase change memories.

RESULTS AND DISCUSSION

We investigate the phase change between the semiconducting 2H and semi-metallic 1T′ phase of $MoTe_2$ for flake thicknesses ranging from the monolayer to ∼104 layers (73 nm), which we consider bulk-like as far as electronic and spectroscopic properties (indirect to direct band gap transition, Raman peak intensities and positions),[24] in spite of still being optically thin. Charge injection into $MoTe_2$ is realized using a gated DEME-TFSI ionic liquid because it has been shown to be able to generate a sufficiently large electron charge density ($>1 \times 10^{14}$ cm^{-2})[18,20] to induce the phase change (Figure 1b, see Materials and Methods section). Since the 2H and 1T′ phases exhibit different crystal structures, they also have distinct phonon modes. As a result, we probe the phase change using *in situ* Raman spectroscopy. Notation of the 2H and 1T′ $MoTe_2$ Raman modes is clarified in Supplementary Table 1.

Bulk-like Phase Change. Figure 2a shows the Raman spectra during a full gating cycle of a 60 nm $MoTe_2$ flake. At 0 V, the characteristic out-of-plane vibrational mode, 2H A_{1g}, at 173 cm^{-1} and the in-plane vibrational mode, 2H E_{2g}, at 234 cm^{-1} are observed. The low intensity of the A_{1g} peak is characteristic of bulk flakes where the out-of-plane vibrations are dampened by many-layer interactions.[25] The broad peak at 120 cm^{-1} and the range of peaks from 270 to 350 cm^{-1} are due to the DEME cation and TFSI anion of the ionic liquid, respectively (Supplementary Figure 1).[26] As the voltage is increased up to 4.0 V, no significant peak shifts or peak intensity changes are observed in the 2H A_{1g} and 2H E_{2g} peaks.

At 4.0 V, the critical voltage necessary to induce phase change is attained, which is marked by the appearance of an initially small 1T′ A_{1g} peak at 168 cm^{-1}, as highlighted in Figure 2b. The position of this 1T′ Raman peak is consistent with the previous report of electrostatic phase change and corroborates those

https://dx.doi.org/10.1021/acsnano.9b07095
ACS Nano XXXX, XXX, XXX−XXX

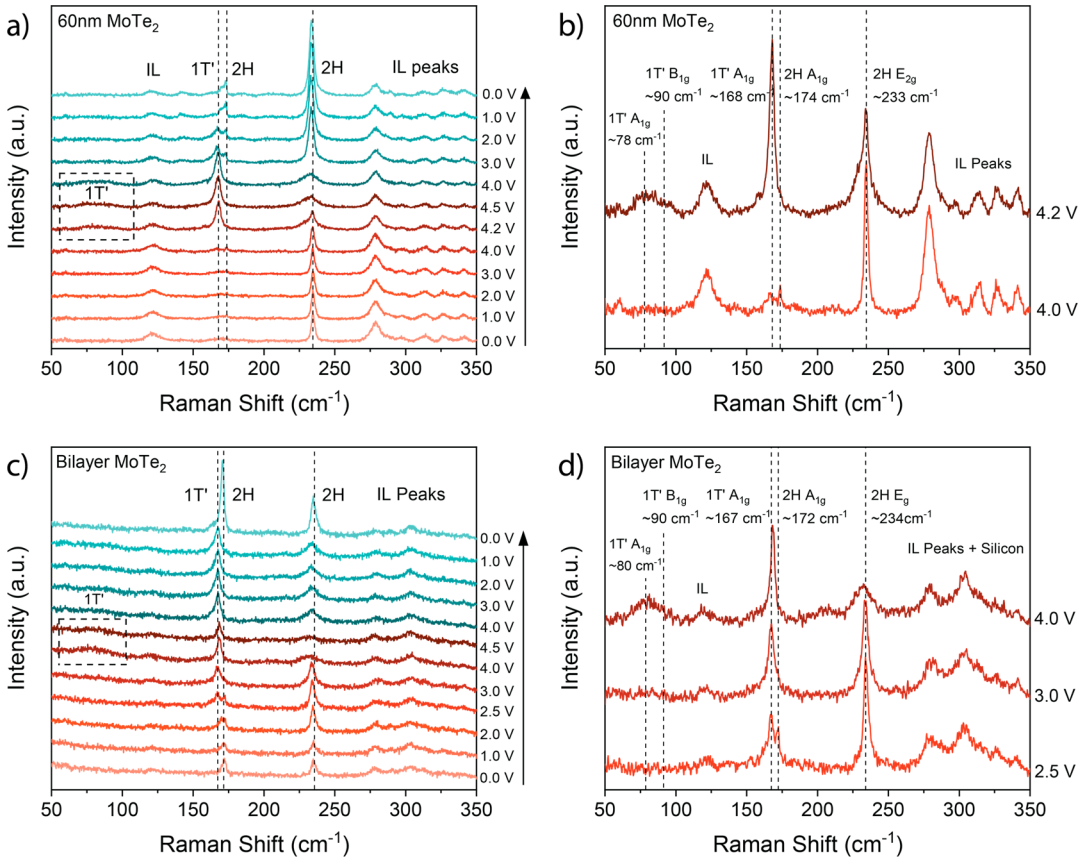

Figure 2. Raman characterization of the 2H to 1T′ $MoTe_2$ phase transition. (a,b) *In situ* Raman progression of a bulk-like 60 nm $MoTe_2$ flake under ionic liquid gating from 0 to 4.5 V to 0 V. (b) The transition voltage at 4.0 V in (a) and the appearance of the 1T′ peaks at ∼78 cm^{-1}, ∼90 cm^{-1}, and ∼168 cm^{-1}. (c,d) *In situ* Raman progression of a bilayer $MoTe_2$ flake under ionic liquid gating from 0 to 4.5 V to 0 V. The spectra are qualitatively like those observed in the bulk-like case. (d) The 2.5 V transition voltage in (c) and the coexistence of the 1T′ and 2H peaks at this voltage.

findings.[18] This voltage marks the beginning of nucleation of 1T′ domains in the 2H flake. A large increase in the 1T′ A_{1g} intensity is observed at 4.2 V, accompanied by a decrease in intensity and broadening of the 2H E_{2g} peak. Concurrently, we observe the rise of additional peaks at ∼78 cm^{-1} and ∼90 cm^{-1}, which we attribute to the A_{1g} and B_{1g} modes of 1T′.[27] These peaks have not been previously observed in 2H to 1T′ $MoTe_2$ phase change experiments but are consistently reported as prominent 1T′ peaks in the DFT and chemical vapor deposition (CVD)-growth literature (Supplementary Table 2). Fundamentally, the line widths of the Raman modes are inversely related to the phonon lifetime, with broader line widths indicating faster phonon decay, generally attributed to an increased number of defects.[28] The broad nature of the 1T′ 78 and 90 cm^{-1} peaks as well as the 2H E_{2g} peaks suggests that upon ionic liquid gating, the 1T′ phase as well as the remaining 2H phase become defective. A discussion of the Raman peak center and line widths as well as their values are included in Supplementary Figures 2 and 3.

Upon removing charge, several effects are observed. At 3 V, the 78 and 90 cm^{-1} peaks disappear, corroborating the fact that they arise from the gate-induced phase transformation and do not come from parasitic chemical reactions. The 168 1T′ peak on the other hand persists but lowers in intensity. This decrease in the 1T′ peak intensity coincides with an increase in the intensity of the 2H E_{2g} peak and A_{1g} peaks beyond their original intensity. The intensity increase is not completely understood at this stage but is most likely due to multiple beam reflection and interference which is a well-documented phenomenon in layered 2D materials. Similar Raman enhancement has been observed in the case of changing substrate thickness under graphene as well as during intercalation of graphene and MoS_2.[29−31] A more detailed discussion of optical interference is included in Supplementary Figures 4−6 and Supplementary Video 1. The increase in intensity makes the 2H A_{1g} peak at 172 cm^{-1} more visible as compared to the initial state, and this signal most likely carries a contribution from 2H layers underneath the 1T′. At 1 V, 1T′ $MoTe_2$ transforms back to the 2H phase with the addition of a shoulder off the ∼172 cm^{-1} 2H A_{1g} peak. We attribute this shoulder to a potential distribution of 2H domains with varying strains and defect densities that arise from phase change cycling. In summary, the phase change process appears to be partially reversible in thick flakes.

Bilayer Phase Change. Building up toward the bulk-like regime described above, a similar pattern of phase change is observed in bilayer $MoTe_2$ as seen in Figure 2c,d. The 2H A_{1g} and 2H E_{2g} peaks start with nearly identical intensities, which is characteristic of bilayer $MoTe_2$.[32] In contrast to the thicker 60 nm MoTe2 flake, phase change in the bilayer $MoTe_2$ occurs at 2.5 V, where coexistence of the 1T′ A_{1g} and 2H A_{1g} is observed (Figure 2d). Unlike the bulk-like case, the 2H E_{2g} peak does not drop in intensity at this transition voltage. It is not until 4 V that the intensity of the 2H E_{2g} drops significantly, the line width broadens, and a broad convolution of the 1T′ peaks at 80 and 90 cm^{-1} appear. Upon discharging the flake, the flake reverts to the

https://dx.doi.org/10.1021/acsnano.9b07095
ACS Nano XXXX, XXX, XXX−XXX

2H phase only at 0 V, indicating that a strong kinetic barrier induces hysteresis, as previously reported.[18] At 0 V, the intensities of the 2H peaks are larger than prior to gating, which we attribute again to an optical interference effect. We also note that the intensity of the 2H A_{1g} peak is higher than that of the 2H E_{2g} peak, which is characteristic of monolayer $MoTe_2$ and indicates thinning of the bilayer to monolayer, but we do not know at what voltage step the thinning occurred. While the Raman laser power (0.52 mW) was selected to minimize heating to temperature changes less than 50° (Supplementary Figure 7), application of large voltages made flakes more susceptible to laser thinning (Supplementary Figure 8). Despite thinning, phase change is not driven by an irreversible laser heating process, as all experiments showed reversibility to the 2H phase after cycling. In either case, a similar pattern of phase change is observed in both bulk-like and bilayer $MoTe_2$

Discussion of Phase Change Mechanism. Throughout the bilayer and bulk-like experiments discussed above, the 2H E_{2g} signal never entirely disappears, indicating coexistence of the 2H and 1T′ phases. The coexistence suggests two possible scenarios. First, the phase change occurs on the top or top-few layers, and the 2H Raman signature originates from underlying layers. Alternatively, the phase change is not complete even on the topmost layers, and the Raman measurement probes both 2H and 1T′ domains on the surface. We hypothesize that what is observed is a combination of both effects.

To investigate whether charge can be transferred from the ionic liquid to layers below the top layer, we perform DFT calculations of a system consisting of a lithium atom sitting on top of a bilayer of 2H $MoTe_2$ (Figure 3). The lithium atom is used as a proxy for the ionic liquid in order to investigate doping of the bilayer with electrons. The quantity of interest is the amount of charge that moves from the lithium atom to the bottom layer. To investigate this, we compute the fractional charge $N(z)$ of the excess electron coming from the lithium atom at location z in the cell for three different lithium atom positions above the bilayer, plotted on the x-axis of Figure 3:

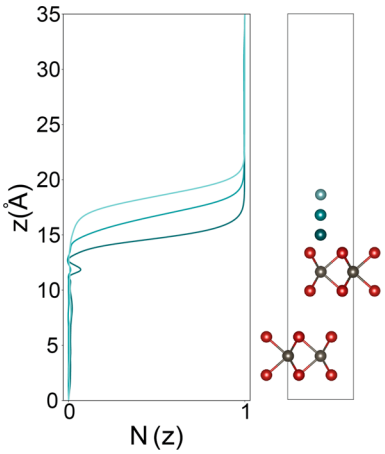

Figure 3. Location of electrostatically doped charge density. Varying the position of a lithium atom on a $MoTe_2$ layer, we find that the DFT-computed excess charge stays almost entirely in the first layer.

$$N(z) = \int_0^z (n_{\mathrm{Li+MoTe_2}}(x', y', z') - n_{\mathrm{MoTe_2}}(x', y', z'))dx'dy'dz'$$

where $n_{\mathrm{Li+MoTe_2}}$ is the charge density of the Li + bilayer system and $n_{\mathrm{MoTe_2}}$ is the charge density of the bilayer. Regardless of the position of the lithium atom with respect to the surface, we find that no appreciable charge density exists past the first layer. Notably, the charge density associated with the excess electron coming from the lithium atom is around 0.25 e/f.u. $MoTe_2$ in these calculations, much higher than the charge density predicted[20] and measured[18] as necessary to cause the transformation, around 0.05 e/f.u. $MoTe_2$. While an idealized case, the DFT results dispel the possibility of a 2H to 1T′ transition in all layers of the sample and supports the idea of a top or top-few layer transition. In the case of a few-layer transition, the DFT studies show charge donation from the top layer to layers below are unlikely to occur in the pristine bilayer case. This suggests that charge donation to layers below must be mediated by local defects in the sample, such as intercalants between layers that mediate charge transfer. Another possibility is that the Te vacancies generated during the gating process allow for mobile Te atoms to mediate charge transfer between layers. In either case, it is unlikely for charge to penetrate more than a few layers below the surface.

However, experimentally, we hypothesize that the ∼80 cm^{-1} 1T′ A_{1g} and ∼90 cm^{-1} 1T′ B_{1g} modes might be indicative of a few-layer phase change, where additional 1T′ layers increase the Raman signal and allow the peaks to be detected, compared to a monolayer. This hypothesis is based on a 2-fold observation that the ∼80 and 90 cm^{-1} 1T′ modes do not always appear and disappear concurrently with the main ∼168 cm^{-1} A_{1g} 1T′ peak, which suggests a layer-by-layer phase change process. Second, the ∼80 and ∼90 cm^{-1} 1T′ peaks do appear and disappear concurrently with the respective decrease and increase of the 2H E_{2g} peaks, indicating that the loss of pristine 2H signal is tied with the appearance of 1T′ peaks. In the bulk-like case, we would expect a large 2H E_{2g} signal from the underlying pristine 2H layers that are not transformed. However, between 4 and 4.5 V, we see that the 2H E_{2g} signal is broad and faint, indicating that pristine 2H is now only found deeper in the flake due to additional layers of phase-changed 1T′ on top. At 3 V, the ∼80 and ∼90 cm^{-1} 1T′ peaks disappear, the ∼168 cm^{-1} 1T′ peak remains, and the 2H E_{2g} peak increases in intensity, suggesting that the underlying layers of 1T′ have changed back to 2H and only the surface layer of 1T′ remains. These observations also hold true in the case of the bilayer experiment, but the ambiguity of when the thinning occurs makes it difficult to confirm such a conclusion. Nevertheless, in the bilayer experiment at 4 V, whether we interpret the spectra as bilayer 1T′ or monolayer 1T′ due to thinning, we still observe that the 2H E_{2g} peak does not fully disappear. This result implies that the 2H to 1T′ phase change is not complete, with regions of defective 2H $MoTe_2$ remaining in a layer. Thus, we suggest that the phase change happens in the top or topmost layers and the extent of the phase change in the lateral direction is not complete.

We also consider the possibility that the phase change is driven by intercalation of the DEME cations into the $MoTe_2$ flakes. However, using *ex situ* X-ray diffraction (XRD), we do not find any evidence of intercalation (Supplementary Figure 9). Furthermore, intercalation is often optically identified by a color change from the edge of a flake to the middle, as the intercalant increases the local thickness of the flake and alters the optical path lengths for interference. However, in our experiments, the color change happens simultaneously over the entire surface of the flake and no moving front is observed (Supplementary Video 1).

Thickness Dependence. In addition to the bilayer and bulk-like cases, phase change was observed in $MoTe_2$ flakes of

https://dx.doi.org/10.1021/acsnano.9b07095
ACS Nano XXXX, XXX, XXX−XXX

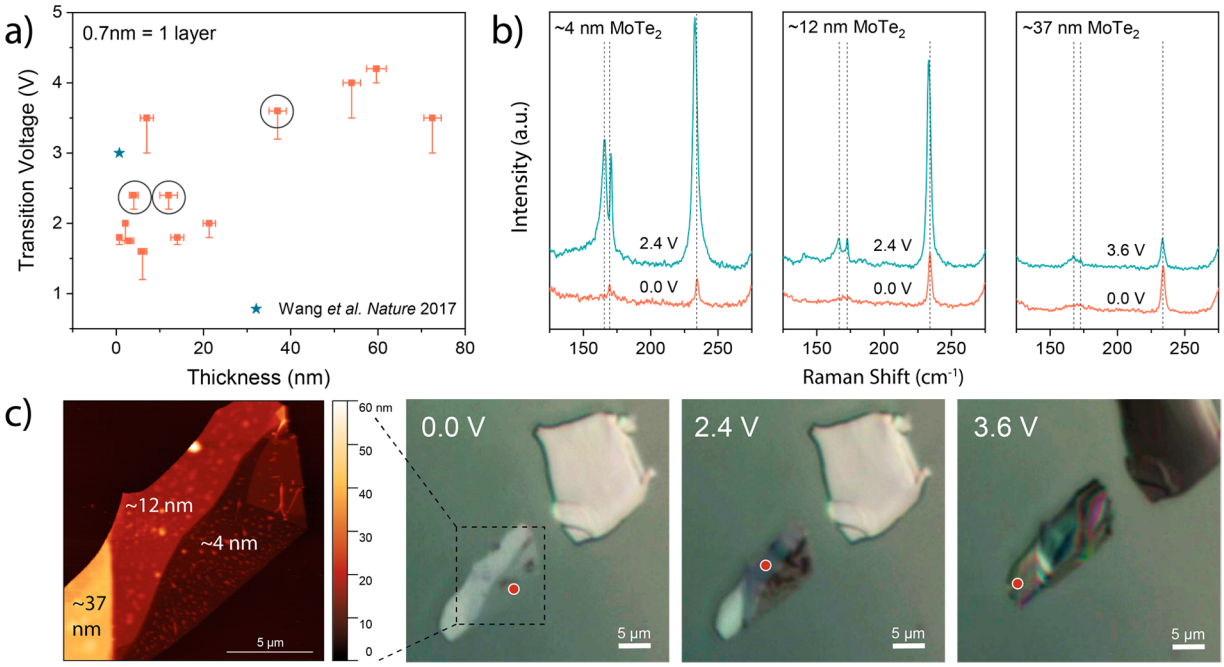

Figure 4. Thickness dependence on the transition voltage. (a) Comparing the 2H to 1T′ transition voltage in $MoTe_2$ flakes of different thicknesses taken from *in situ* Raman measurements. Work by Wang *et al.* on monolayer $MoTe_2$ is shown as reference. The *y*-axis error bars represent voltage steps used in the gating experiments, and the *x*-axis error bars represent uncertainties from AFM measurements. The gray circles highlight the experiments shown in (b,c). (b) The initial and transition voltage Raman spectrum of $MoTe_2$ flakes of different thicknesses, all plotted on the same intensity scale. These spectra correspond to the regions in the optical images in (c) and are marked by a red dot. (c) AFM image showing the ∼4, ∼12, and ∼37 nm regions that are depicted in the three optical images. The optical images show a color change on the regions of the flake associated with their transition voltage.

varying thicknesses (Figure 4a), where we observe that thicker flakes require a larger voltage to induce phase change. The transition voltage is defined as the voltage where the 1T′ peak is first detected in the *in situ* Raman measurements. We highlight three of those thicknesses and show the Raman spectra at the transition voltage in Figure 4b and the atomic force microscopy (AFM) and optical images of the corresponding flake in Figure 4c. In the Raman spectrum, we see that the 4 and 12 nm regions of the flake both undergo phase change at 2.4 V with the appearance of the 1T′ peak. Yet again, we see a sharp increase in the intensity of all the peaks, which we attribute to Raman enhancement from optical interference. In the 37 nm region of the flake, phase change only occurs at 3.6 V, and we do not see an increased Raman signal, making the phase change difficult to distinguish. The optical images, taken during the measurement, serve to illustrate the phase change with distinct coloration occurring at the transition voltages. However, we note that the coloration is explained by thin-film interference effects due to the ionic liquid and does not come from the 1T′ phase but appears coincidentally (see supplementary discussion on optical interference). The images visually confirm the thickness dependence on the transition voltage, with the 4 and 12 nm regions changing color at 2.4 V, but the 37 nm region only changing color at 3.6 V.

In the case of few-layer flakes, where interlayer interactions can lead to Davydov peak splitting, it is important to distinguish the gate-induced 1T′ peak from a potential Davydov peak. In Supplementary Figure 10, we show how the spectral features of the 1T′ peak are distinct from Davydov peaks, disproving potential concerns of peak misidentification. Given the observed phase change phenomena in a variety of thicknesses, we hypothesize that the phase change is electrochemically mediated through the creation of Te vacancies.

Electrochemical Phase Change by Creation of Te Vacancies. Raman characterization of the $MoTe_2$ flakes revealed the presence of Te metal either on or around the $MoTe_2$ flakes at the end of the gating process. Figure 5 shows a series of Raman maps highlighting the presence of a Te metal film next to a $MoTe_2$ flake. Representative spectra from the Raman maps are plotted in Figure 5e displaying the characteristic Te metal peaks[33,34] at ∼120 cm^{-1} and ∼140 cm^{-1} as well as the 2H E_{2g} $MoTe_2$ and silicon peaks. The presence of Te away from $MoTe_2$ flakes is further confirmed by Auger spectroscopy in Supplementary Figure 11.

The mechanism for the formation of Te by electrolysis is well-documented and was first demonstrated by Ernyei in 1900 and Dennis and Anderson in 1914. They showed that the reduction of a Te cathode in dilute acid will form H_2Te gas which spontaneously decomposes at room temperature with O_2 to reform elemental Te and water.[35,36] Recently, electrolysis of layered Bi_2Te_3 in dilute acid was found to create Te nanowires *via* the decomposition of H_2Te.[37,38] The reduction of our $MoTe_2$ is analogous, where hydrogen ions react with $MoTe_2$ to form H_2Te which then decomposes into Te due to measurement conditions in air. The source of hydrogen ions comes either from the electrolysis of adventitious water absorbed in the ionic liquid or from the ionic liquid itself where Hope *et al.* showed that ionic liquids can deprotonate during gating.[39] Because the p++ Si electrode is used as a universal contact, electrically connecting every flake on the substrate, H_2Te can be generated at all $MoTe_2$ flakes on the substrate and not solely from the flake in the image. Since the formation of Te is dependent on encountering O_2, the Te metal is not favored to form in any specific location and can

https://dx.doi.org/10.1021/acsnano.9b07095
ACS Nano XXXX, XXX, XXX−XXX

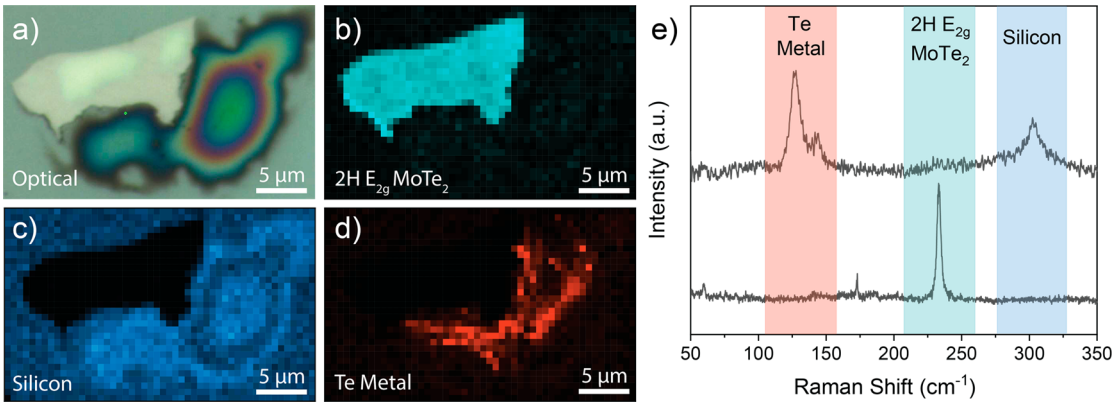

Figure 5. Formation of tellurium metal. (a) Optical image of a $MoTe_2$ flake after most of the ionic liquid was removed at the end of a gating cycle. Raman maps of (b) the $MoTe_2$ flake as shown through the 2H E_{2g} peak, (c) the silicon substrate, and (d) the Te metal as shown through the characteristic ∼120 and ∼140 cm^{-1} peaks. (e) A legend to show what Raman peaks are plotted in the Raman maps.

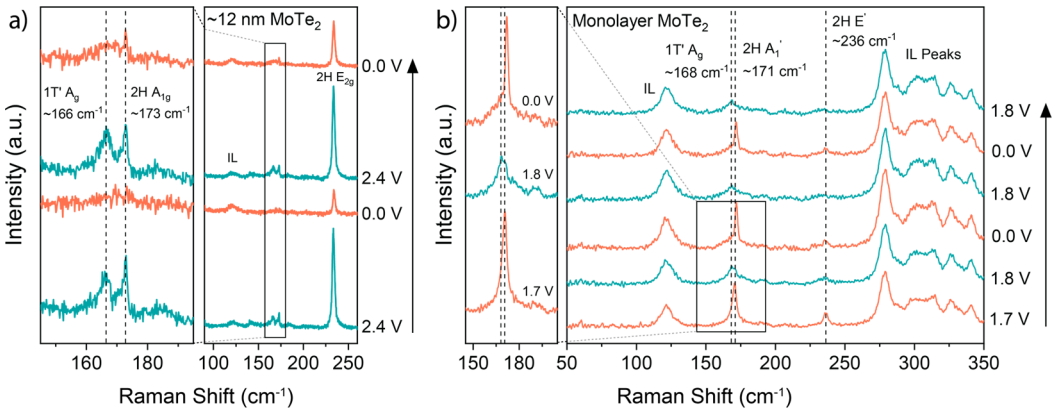

Figure 6. $MoTe_2$ phase cycling. (a) Reversibility in 12 nm $MoTe_2$ where the 2H to 1T′ transition happens at 2.4 V. The inset highlights the 2H and 1T′ peaks, while the zoomed-out portion shows there is an intensity enhancement at 2.4 V. (b) Reversibility in monolayer $MoTe_2$ with the transition voltage at 1.8 V. The peaks are named according to crystal symmetry convention as clarified in the Supporting Information. The inset shows one cycle of phase switching and highlights the shoulder of the 2H A_1' peak after reducing the voltage to 0.0 V.

form far away from the location of measurement. Ultimately, because the $MoTe_2$ flakes are the only source of Te in the experiment, the observation of metallic Te and lack of any observable Mo species proves the formation of Te vacancies in the flakes.

Importantly, Te vacancies can play a crucial role in reducing the energy difference between the 2H and 1T′ phases due to their role as n-type dopants or stabilizing gap states.[22,40] Reported DFT calculations suggest that $MoTe_2$ flakes with Te vacancy concentrations >2% are more stable in the 1T′ phase than in the 2H phase.[22] Experimentally, studies on the CVD growth of $MoTe_2$ found that tellurization of a Mo/MoO_3 film resulted in the 1T′ phase in Te-deficient conditions, while it favored the 2H phase in excess Te conditions.[16,21] Furthermore, Keum *et al.* demonstrated that the transformation temperature from the 2H to the 1T′ phase decreased to ∼650 °C from ∼820 °C in Te-deficient $MoTe_2$.[23] Computational and experimental evidence support the conclusion that Te-deficient $MoTe_2$ favors the 1T′ phase.

To further investigate the role of Te vacancy formation, we explore the effect of Te vacancies on the Raman modes used to identify 1T′ $MoTe_2$ through DFT-based methods. We compute the phonon modes of pristine and ∼3% Te-deficient $MoTe_2$ (see Materials and Methods section). The results indicate that even with a relatively high 3% Te vacancy concentration, the calculated Raman active A_g mode of the 1T′ phase at 163 cm^{-1} remains remarkably similar in frequency and vibrational pattern to the A_g mode of pristine $MoTe_2$ (Supplementary Figure 12). This suggests that the Raman spectra found in experiments would not be sensitive enough to detect Te vacancy formation *via* a frequency shift in the active A_g mode.

These observations lead us to hypothesize that the mechanism of phase change in $MoTe_2$ flakes in our experiments has both an electrochemical and an electrostatic component. In fact, it is now understood that transistor control through electrolyte gating is not fully explained by electrostatic induction of carriers and can proceed *via* electrochemical mechanisms.[41] For example, electrochemical mechanisms evidenced by the formation of oxygen vacancies have been reported in a number of oxide systems such as VO_2, $La_{1-x}Sr_xCoO_{3-\delta}$, and $SrTiO_3$.[41] In our case, we have a chalcogenide system where we speculate that the electrochemical creation of Te vacancies during electrolyte gating lowers the energy difference between 2H and 1T′ and the simultaneous electrostatic doping drives the transition.

Reversibility. Even though the phase change is mediated by tellurium vacancies, the phase transformation process retains an electrostatic component. The reversible nature of the phase change in the 12 nm $MoTe_2$ flake previously discussed is displayed in Figure 6a. The 1T′ Ag peak disappears upon decreasing the voltage to 0 V and reappears upon gating back to

https://dx.doi.org/10.1021/acsnano.9b07095
ACS Nano XXXX, XXX, XXX−XXX

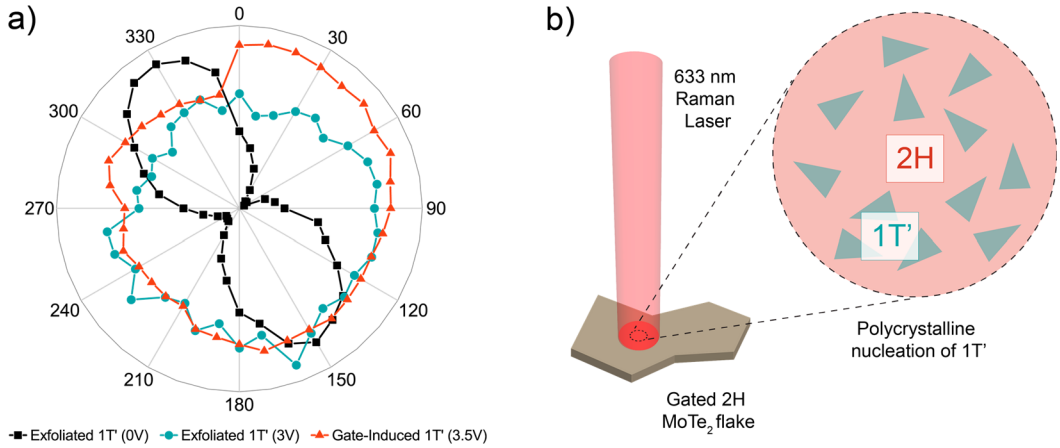

Figure 7. Isotropic 1T′ nucleation. (a) Comparing polarization-resolved Raman of the 1T′ A_{1g} peak between pristine, exfoliated 1T′ at 0 and 3 V, and gate-induced 1T′ from a 2H flake. The exfoliated 1T′ was gated in the same gating conditions as all other experiments. (b) Schematic depicting the polycrystalline nucleation of 1T′ domains in a 2H layer that would lead to the loss of polarization dependence seen in the gate-induced 1T′ (3.5 V) of (a).

2.4 V. Since this is a thicker flake, the 2H A_{1g} peak is known to be hard to distinguish, but the wider range scan shows the presence of the 2H E_{2g} to confirm the 2H nature of the flake. Figure 6b shows reversible phase switching of a monolayer $MoTe_2$ flake. The characteristic signature of monolayer 2H $MoTe_2$ where the A_1' is higher in intensity than the E′ peak is visible.[25] The sharp 2H A_1' peak disappears and the broad 1T′ A_g peak appears upon gating to 1.8 V. The 2H E′ peak also disappears, indistinguishable from the noise. After cycling back to 0 V, we see the 2H peaks return, but differing in intensity and peak position. Additionally, a shoulder on the 2H A_1' peak appears (Figure 6b inset). These observations point to possible defect formation and the partial reversibility of the process.

Heterogeneous Nucleation of 1T′ Domains. The breadth of the 1T′ Raman peak and the broadening of the 2H peaks upon cycling suggest that the single crystal nature of the material is perturbed during the gating process. In order to test the in-plane crystalline texture of the gate-induced 1T′ $MoTe_2$, we investigated the polarization dependence of the 1T′ A_{1g} peak. Symmetry analysis of the 1T′ A_{1g} mode shows that the 1T′ A_{1g} mode has anisotropic scattering components that result in a two-lobe pattern in polarized Raman measurements (Figure 7a). In contrast, in our gate-induced 1T′, there is no polarization dependence, suggesting that the resulting 1T′ is polycrystalline with domains forming along different crystallographic directions within the Raman spot size (Figure 7b). This result contrasts with work by Wang *et al.*, who demonstrated the characteristic two-lobe pattern in their gate-induced 1T′ at 220 K and in vacuum, indicating single crystal 1T′.[18] We speculate that the loss of polarization dependence is due to the formation of Te vacancies and the electrochemical contribution to the transformation process observed here, which allow the 1T′ to nucleate isotropically. This hypothesis is supported by a recent ultrahigh-vacuum scanning tunneling microscopy report of 2H $MoTe_2$ after a 400 °C thermal treatment which showed the presence of 60° inversion domain boundaries and was explained by Te vacancy creation.[42] We tested this assumption by performing the same gating conditions on a pristine 1T′ flake exfoliated from a commercially obtained source. The initial polarization dependence of the exfoliated 1T′ is lost after gating past 3 V. These results indicate that the electrolyte gating process allows the $MoTe_2$ surface to reorganize, which explains why our gate-induced 1T′ does not exhibit any polarization dependence.

CONCLUSION

We report evidence of 2H to 1T′ phase change in $MoTe_2$ flakes upon ionic liquid gating at room temperature and ambient conditions in flake thicknesses ranging from monolayer to bulk-like (73 nm). We find that the phase change is partially reversible through electrostatic doping and also electrochemically mediated by the creation of Te vacancies, which is supported by the observation of Te metal formation. The process leaves a mixture of phases, as not all of the 2H in a given layer is transformed to 1T′, with the transformation possibly occurring beyond the first layer. Furthermore, the 1T′ domains are nucleated with varying crystalline orientations which results in a loss of the polarization dependence of the 1T′ Raman spectrum.

This is the second report of voltage-induced phase change in $MoTe_2$. While the previous report showed the phase change at 220 K and in vacuum, our observation of reversible phase change at room temperature and ambient conditions is relevant for implementation of $MoTe_2$ in phase change memory devices. This work also highlights the simultaneous activation of an electrochemical and an electrostatic switching mechanism as well as the important role of Te defects and the necessity of better understanding them. Pretreatment of $MoTe_2$ devices to induce Te defects by annealing, plasma bombardment, or electrochemical dissociation may be a way to tune the transition voltage into a desirable range for phase change memory applications.

MATERIALS AND METHODS

Exfoliation of $MoTe_2$, MoS_2, and WTe_2 Flakes. 2H and 1T′ $MoTe_2$, 2H MoS_2, and 1T′ WTe_2 flakes were mechanically exfoliated from commercially purchased bulk crystals from HQ graphene using 3M 810 Magic Tape or Blue Medium 18074 Thermal Release Tape from Semiconductor Equipment Corp. All exfoliations were done in air, and the peel back of the tape was done quickly. A quick rip was qualitatively found to produce higher yields of few-layer $MoTe_2$ flakes. The exfoliated flakes were either directly applied to a p++ silicon substrate for testing or first transferred to a PDMS stamp to be then stamped onto the silicon substrate. When transferring from PDMS to the silicon substrate, the PDMS was put into contact with the substrate and then heated to 40 °C for 2 min before being ripped off.

https://dx.doi.org/10.1021/acsnano.9b07095
ACS Nano XXXX, XXX, XXX−XXX

Thickness Determination of $MoTe_2$ Flakes. The thickness of the $MoTe_2$ flakes was determined by a combination of optical microscopy, AFM, and Raman spectroscopy. First, promising monolayer to few-layer regions were identified by microscope based on optical contrast. Then the thickness of the identified flake was measured using noncontact AFM in a Park XE-100. Since it is well documented that a 1−2 nm interfacial layer of residue can exist between the substrate and 2D material,[43] the AFM results were corroborated by looking at the Raman signature of the flake. Monolayer to five-layer flakes of $MoTe_2$ can be distinguished by the ratio of the Raman A_{1g} and B_{2g} peaks.[25] The combined AFM + Raman was important for unambiguous determination of thin flakes. However, for thicker flakes, the AFM result was used, and the 1−2 nm uncertainty was wrapped up in the error.

Storage of Ionic Liquid and Preparation of CTAB. DEME-TFSI and 1-ethyl-3-methylimidazolium tetrafluoroborate (EMI-BF_4) were purchased from Iolitec and stored in a nitrogen glovebox. Before transferring into the glovebox, the ionic liquid was first dried in a vacuum oven at 80 °C for 24 h to remove any water that might have been introduced during the shipping process. Small volumes of DEME-TFSI and EMI-BF_4 were removed from the glovebox on an experiment by experiment basis. Cetyltrimethylammonium bromide (CTAB) was purchased from Sigma-Aldrich and stored in air. Saturated CTAB electrolyte was made in *N*-methyl-2-pyrrolidone.

Preparation of the Gating Cell. The gating cell was built to be easily implemented, disposable, and cheap. No lithography or metal deposition was used in the construction of the cell. The cell consists of two electrodes: a three-dimensional (3D)-printed exterior well and a 3D-printed interior well capped at one end with a quartz coverslip. At the end of the exfoliation process mentioned above, the $MoTe_2$ flake rests on polished, p++ doped silicon which acts both as a substrate and electrode. The 3D-printed exterior well is epoxied (Lysol 1H) onto the p++ silicon such that the $MoTe_2$ flake of interest is in the center of the well. The epoxy cures overnight at room temperature in a nitrogen box to minimize oxygen exposure to the $MoTe_2$. The counter-electrode or gate is a gold wire that is coiled to rest inside of the exterior well and propped up such that it does not touch the p++ Si substrate. Approximately 300 μL of DEME-TFSI is added to the exterior well, and the interior well is then placed inside of the exterior well, displacing a large volume of the ionic liquid and allowing a liquid-free path to the $MoTe_2$ flake for the Raman laser. The quartz coverslip of the interior well presses up against the $MoTe_2$ flake and Si substrate, forming a thin interfacial layer of ionic liquid that minimizes unwanted scattering but can still rearrange its ions to react to the applied electric field. After measurement, the gold wire and interior well are washed with repeated rinses of isopropyl alcohol and water and can be used again.

The height of the gating cell is 6 mm and was chosen to be smaller than the working distance of the 100× LWD objective used in the Raman experiments. The diameter of the exterior cell is 12 mm, and the diameter of the interior well is 8 mm. The length of the gold wire was chosen to have a higher surface area then the area of the p++ silicon electrode.

Oxygen Exposure of $MoTe_2$. $MoTe_2$ is known to be moderately oxygen sensitive on the order of hours to days.[44] The $MoTe_2$ exfoliation tapes and prepared substrates are stored in a nitrogen box to minimize exposure. The estimated total air exposure during experimental preparation is 3−4 h. No signs of oxidation peak have been found in Raman measurements prior the gating.

***In situ* Raman measurements.** The *in situ* Raman gating experiments were performed using a Horiba Labram Evolution with a 633 nm laser and a 100× LWD (0.6 NA) objective. All experiments were done in ambient conditions. A laser power of 0.52 mW was chosen to minimize thermal heating (see Supplementary Figure 7). A Keithley 2400 was used at the voltage source, and contacts were made by means of XYZ micromanipulator probes and alligator clips. An 1800 g/mm was used to maximum peak resolution, and the Raman region of 50−350 cm^{-1} was studied. Measurements times and accumulations varied but were generally a 10 s acquisition with 6 accumulations or a 30 s acquisition with 3 accumulations. When the voltage was changed, the ions were given 30−60 s to equilibrate before the Raman measurement was started.

Polarized Raman Measurements. Polarized-resolved Raman was achieved by using a 633 nm half-wave plate mounted before the objective to rotate the incident linearly polarized light. No additional polarizers were used after the objective, and the Raman signal was collected in reflected mode by the Silicon CCD.

Auger Measurements. Auger measurements were performed using a PHI 700 Scanning Auger Nanoprobe at 10 keV and 10 nA. The dominant Te MNN transition at 486 eV was used to identify the location of Te.

DFT Calculations. All DFT calculations were performed using the Vienna *ab Initio* Simulation Package,[45−48] version 5.4.4. All calculations use PAW pseudopotentials to treat the core electrons.[49,50] The lithium atom on bilayer $MoTe_2$ calculations were performed using 4 formula units of $MoTe_2$ (an orthorhombic cell consisting of 2 formula units on each layer). To accurately treat the potential between layers which has a van der Waals component, we use the SCAN + rVV10[51,52] functional. For these calculations, an energy cutoff of 400 eV is used. Atom positions are allowed to relax in the bilayer. We use tetrahedral integration of the Brillouin zone with a smearing parameter of 0.05 eV and an energy cutoff of 10^{-4} eV.

For calculations of vibrational modes, we use the PBE GGA functional,[53] along with the Phonopy[54] package to analyze the vibrational modes. A 16 f.u. cell of $MoTe_2$ with a 400 eV cutoff and 10^{-5} eV energy convergence threshold are used, along with Gaussian smearing with a 0.05 eV smearing width. Phonon modes are computed using the built-in density functional perturbation theory method implemented in VASP.

All input files for calculations can be found as a zip file in the Supporting Information.

ASSOCIATED CONTENT

Supporting Information

The Supporting Information is available free of charge at https://pubs.acs.org/doi/10.1021/acsnano.9b07095.

Nomenclature of phonon modes, comparison of 2H and 1T′ Raman peaks in literature, Raman signature of DEME-TFSI and the Si substrate, peak centers and line widths of Raman data, discussion of optical interference with respect to Raman enhancement and color changes, estimations of laser heating evidence of thinning of few-layer flakes, investigation of intercalation using XRD, phase change in 3−4L flake, Auger mapping, and DFT analysis of 1T′ modes with vacancies (PDF)

Video 1: Optical video feed of an $MoTe_2$ flake during *in-situ* Raman gating that highlights the formation of varying thicknesses of the ionic liquid electrolyte that gives rise to optical interference. (MP4)

Input files for the DFT calculations that investigate the amount of charge transferred from a Li atom to the bottom layer of bilayer 2H $MoTe_2$ (ZIP)

AUTHOR INFORMATION

Corresponding Author

Alberto Salleo − *Department of Materials Science and Engineering, Stanford University, Stanford, California 94305, United States*; Email: asalleo@stanford.edu

Authors

Dante Zakhidov − *Department of Materials Science and Engineering, Stanford University, Stanford, California 94305, United States*; orcid.org/0000-0003-3107-104X

Daniel A. Rehn − *Department of Mechanical Engineering, Stanford University, Stanford, California 94305, United States; Computational Physics Division and Theoretical Division, Los Alamos*

https://dx.doi.org/10.1021/acsnano.9b07095
ACS Nano XXXX, XXX, XXX−XXX

National Laboratory, Los Alamos, New Mexico 87545, United States; orcid.org/0000-0001-5139-0393

Evan J. Reed − *Department of Materials Science and Engineering, Stanford University, Stanford, California 94305, United States*

Complete contact information is available at: https://pubs.acs.org/10.1021/acsnano.9b07095

Notes

The authors declare no competing financial interest.

This article was initially submitted to the arXiv pre-print repository in the condensed matter, materials science section under article number arXiv:1905.12746.[55]

ACKNOWLEDGMENTS

Part of this work was performed at the Stanford Nano Shared Facilities (SNSF), supported by the National Science Foundation under award ECCS-1542152. This work was also partially supported by NSF grant nos. ECCS-1436626 and DMR-1455050, Army Research Office grant no. W911NF-15-1-0570, Office of Naval Research grant no. N00014-15-1-2697, and a seed grant from Stanford SystemX Alliance. This work was supported in part by the US Army Research Laboratory, through the Army High Performance Computing Research Center, cooperative agreement no. W911NF-07-0027. The authors would like to thank A. R. Chew, Y. Li, and O. B. Aslan for helpful discussion. D.Z. acknowledges support by the National Science Foundation Graduate Research Fellowship under grant no. DGE-1656518.

REFERENCES

(1) Geim, A. K.; Novoselov, K. S. The Rise of Graphene. *Nat. Mater.* **2007**, *6*, 183−191.

(2) Molle, A.; Goldberger, J.; Houssa, M.; Xu, Y.; Zhang, S.-C.; Akinwande, D. Buckled Two-Dimensional Xene Sheets. *Nat. Mater.* **2017**, *16*, 163−169.

(3) Anasori, B.; Lukatskaya, M. R.; Gogotsi, Y. 2D Metal Carbides and Nitrides (MXenes) for Energy Storage. *Nat. Rev. Mater.* **2017**, *2*, 16098.

(4) Hantanasirisakul, K.; Gogotsi, Y. Electronic and Optical Properties of 2D Transition Metal Carbides and Nitrides (MXenes). *Adv. Mater.* **2018**, *30*, 1804779.

(5) Chhowalla, M.; Shin, H. S.; Eda, G.; Li, L.-J.; Loh, K. P.; Zhang, H. The Chemistry of Two-Dimensional Layered Transition Metal Dichalcogenide Nanosheets. *Nat. Chem.* **2013**, *5*, 263−275.

(6) Manzeli, S.; Ovchinnikov, D.; Pasquier, D.; Yazyev, O. V.; Kis, A. 2D Transition Metal Dichalcogenides. *Nat. Rev. Mater.* **2017**, *2*, 17033.

(7) Rehn, D. A.; Li, Y.; Pop, E.; Reed, E. J. Theoretical Potential for Low Energy Consumption Phase Change Memory Utilizing Electrostatically-Induced Structural Phase Transitions in 2D Materials. *Npj Comput. Mater.* **2018**, *4*, 2.

(8) Rehn, D. A.; Li, Y.; Reed, E. J. Refrigeration in 2D: Electrostaticaloric Effect in Monolayer Materials. *Phys. Rev. Mater.* **2018**, *2*, 114004.

(9) Duerloo, K.-A. N.; Li, Y.; Reed, E. J. Structural Phase Transitions in Two-Dimensional Mo- and W-Dichalcogenide Monolayers. *Nat. Commun.* **2014**, *5*, 4214.

(10) Xiong, F.; Wang, H.; Liu, X.; Sun, J.; Brongersma, M.; Pop, E.; Cui, Y. Li Intercalation in MoS_2: *In Situ* Observation of Its Dynamics and Tuning Optical and Electrical Properties. *Nano Lett.* **2015**, *15*, 6777−6784.

(11) Jin, W.; Schiros, T.; Lin, Y.; Ma, J.; Lou, R.; Dai, Z.; Yu, J.-X.; Rhodes, D.; Sadowski, J. T.; Tong, X.; Qian, T.; Hashimoto, M.; Lu, D.; Dadap, J. I.; Wang, S.; Santos, E. J. G.; Zang, J.; Pohl, K.; Ding, H.; Hone, J.; et al. Phase Transition and Electronic Structure Evolution of $MoTe_2$ Induced by W Substitution. *Phys. Rev. B: Condens. Matter Mater. Phys.* **2018**, *98*, 144114.

(12) Oliver, S. M.; Beams, R.; Krylyuk, S.; Kalish, I.; Singh, A. K.; Bruma, A.; Tavazza, F.; Joshi, J.; Stone, I. R.; Stranick, S. J.; Davydov, A. V.; Vora, P. M. The Structural Phases and Vibrational Properties of $Mo_{1-x}W_xTe_2$ Alloys. *2D Mater.* **2017**, *4*, 045008.

(13) Song, S.; Keum, D. H.; Cho, S.; Perello, D.; Kim, Y.; Lee, Y. H. Room Temperature Semiconductor−Metal Transition of $MoTe_2$ Thin Films Engineered by Strain. *Nano Lett.* **2016**, *16*, 188−193.

(14) Hou, W.; Azizimanesh, A.; Sewaket, A.; Peña, T.; Watson, C.; Liu, M.; Askari, H.; Wu, S. M. Strain-Based Room-Temperature Non-Volatile $MoTe_2$ Ferroelectric Phase Change Transistor. *Nat. Nanotechnol.* **2019**, *14*, 668−673.

(15) Zhang, F.; Zhang, H.; Krylyuk, S.; Milligan, C. A.; Zhu, Y.; Zemlyanov, D. Y.; Bendersky, L. A.; Burton, B. P.; Davydov, A. V.; Appenzeller, J. Electric-Field Induced Structural Transition in Vertical $MoTe_2$- and $Mo_{1-x}W_xTe_2$-Based Resistive Memories. *Nat. Mater.* **2019**, *18*, 55−61.

(16) Park, J. C.; Yun, S. J.; Kim, H.; Park, J.-H.; Chae, S. H.; An, S.-J.; Kim, J.-G.; Kim, S. M.; Kim, K. K.; Lee, Y. H. Phase-Engineered Synthesis of Centimeter-Scale 1T′- and 2H-Molybdenum Ditelluride Thin Films. *ACS Nano* **2015**, *9*, 6548−6554.

(17) Cho, S.; Kim, S.; Kim, J. H.; Zhao, J.; Seok, J.; Keum, D. H.; Baik, J.; Choe, D.-H.; Chang, K. J.; Suenaga, K.; Kim, S. W.; Lee, Y. H.; Yang, H. Phase Patterning for Ohmic Homojunction Contact in $MoTe_2$. *Science* **2015**, *349*, 625−628.

(18) Wang, Y.; Xiao, J.; Zhu, H.; Li, Y.; Alsaid, Y.; Fong, K. Y.; Zhou, Y.; Wang, S.; Shi, W.; Wang, Y.; Zettl, A.; Reed, E. J.; Zhang, X. Structural Phase Transition in Monolayer $MoTe_2$ Driven by Electrostatic Doping. *Nature* **2017**, *550*, 487−491.

(19) Duerloo, K.-A. N.; Reed, E. J. Structural Phase Transitions by Design in Monolayer Alloys. *ACS Nano* **2016**, *10*, 289−297.

(20) Li, Y.; Duerloo, K.-A. N.; Wauson, K.; Reed, E. J. Structural Semiconductor-to-Semimetal Phase Transition in Two-Dimensional Materials Induced by Electrostatic Gating. *Nat. Commun.* **2016**, *7*, 10671.

(21) Zhou, L.; Zubair, A.; Wang, Z.; Zhang, X.; Ouyang, F.; Xu, K.; Fang, W.; Ueno, K.; Li, J.; Palacios, T.; Kong, J.; Dresselhaus, M. S. Synthesis of High-Quality Large-Area Homogenous 1T′ $MoTe_2$ from Chemical Vapor Deposition. *Adv. Mater.* **2016**, *28*, 9526−9531.

(22) Young, J.; Reinecke, T. L. Controlling the H to T′ Structural Phase Transition *via* Chalcogen Substitution in $MoTe_2$ Monolayers. *Phys. Chem. Chem. Phys.* **2017**, *19*, 31874−31882.

(23) Keum, D. H.; Cho, S.; Kim, J. H.; Choe, D.-H.; Sung, H.-J.; Kan, M.; Kang, H.; Hwang, J.-Y.; Kim, S. W.; Yang, H.; Chang, K. J.; Lee, Y. H. Bandgap Opening in Few-Layered Monoclinic $MoTe_2$. *Nat. Phys.* **2015**, *11*, 482−486.

(24) Lezama, I. G.; Arora, A.; Ubaldini, A.; Barreteau, C.; Giannini, E.; Potemski, M.; Morpurgo, A. F. Indirect-to-Direct Band Gap Crossover in Few-Layer $MoTe_2$. *Nano Lett.* **2015**, *15*, 2336−2342.

(25) Ruppert, C.; Aslan, O. B.; Heinz, T. F. Optical Properties and Band Gap of Single- and Few-Layer $MoTe_2$ Crystals. *Nano Lett.* **2014**, *14*, 6231−6236.

(26) Lassègues, J. C.; Grondin, J.; Holomb, R.; Johansson, P. Raman and *Ab Initio* Study of the Conformational Isomerism in the 1-Ethyl-3-Methyl-Imidazolium Bis(Trifluoromethanesulfonyl)Imide Ionic Liquid. *J. Raman Spectrosc.* **2007**, *38*, 551−558.

(27) Beams, R.; Cançado, L. G.; Krylyuk, S.; Kalish, I.; Kalanyan, B.; Singh, A. K.; Choudhary, K.; Bruma, A.; Vora, P. M.; Tavazza, F.; Davydov, A. V.; Stranick, S. J. Characterization of Few-Layer 1T′ $MoTe_2$ by Polarization-Resolved Second Harmonic Generation and Raman Scattering. *ACS Nano* **2016**, *10*, 9626−9636.

(28) Li, T.; Zhang, Z.; Zheng, W.; Lv, Y.; Huang, F. A Possible High-Mobility Signal in Bulk $MoTe_2$: Temperature Independent Weak Phonon Decay. *AIP Adv.* **2016**, *6*, 115207.

(29) Yoon, D.; Moon, H.; Son, Y.-W.; Choi, J. S.; Park, B. H.; Cha, Y. H.; Kim, Y. D.; Cheong, H. Interference Effect on Raman Spectrum of Graphene on SiO_2/Si. *Phys. Rev. B: Condens. Matter Mater. Phys.* **2009**, *80*, 125422.

(30) Jung, N.; Crowther, A. C.; Kim, N.; Kim, P.; Brus, L. Raman Enhancement on Graphene: Adsorbed and Intercalated Molecular Species. *ACS Nano* **2010**, *4*, 7005−7013.
(31) Guo, Y.; Sun, D.; Ouyang, B.; Raja, A.; Song, J.; Heinz, T. F.; Brus, L. E. Probing the Dynamics of the Metallic-to-Semiconducting Structural Phase Transformation in MoS_2 Crystals. *Nano Lett.* **2015**, *15*, 5081−5088.
(32) Guo, H.; Yang, T.; Yamamoto, M.; Zhou, L.; Ishikawa, R.; Ueno, K.; Tsukagoshi, K.; Zhang, Z.; Dresselhaus, M. S.; Saito, R. Double Resonance Raman Modes in Monolayer and Few-Layer $MoTe_2$. *Phys. Rev. B: Condens. Matter Mater. Phys.* **2015**, *91*, 205415.
(33) Huang, J.-H.; Deng, K.-Y.; Liu, P.-S.; Wu, C.-T.; Chou, C.-T.; Chang, W.-H.; Lee, Y.-J.; Hou, T.-H. Large-Area 2D Layered $MoTe_2$ by Physical Vapor Deposition and Solid-Phase Crystallization in a Tellurium-Free Atmosphere. *Adv. Mater. Interfaces* **2017**, *4*, 1700157.
(34) Churchill, H. O. H.; Salamo, G. J.; Yu, S.-Q.; Hironaka, T.; Hu, X.; Stacy, J.; Shih, I. Toward Single Atom Chains with Exfoliated Tellurium. *Nanoscale Res. Lett.* **2017**, *12*, 488.
(35) Ernyei, E. Über Den Tellurwasserstoff. *Z. Für Anorg. Chem.* **1900**, *25*, 313−317.
(36) Dennis, L. M.; Anderson, R. P. Hydrogen Telluride and The Atmoic Weight of Tellurium. *J. Am. Chem. Soc.* **1914**, *36*, 882−909.
(37) Tsai, H.-W.; Yaghoubi, A.; Chan, T.-C.; Wang, C.-C.; Liu, W.-T.; Liao, C.-N.; Lu, S.-Y.; Chen, L.-J.; Chueh, Y.-L. Electrochemical Synthesis of Ultrafast and Gram-Scale Surfactant-Free Tellurium Nanowires by Gas−Solid Transformation and Their Applications as Supercapacitor Electrodes for *p*-Doping of Graphene Transistors. *Nanoscale* **2015**, *7*, 7535−7539.
(38) Tsai, H.-W.; Wang, T.-H.; Chan, T.-C.; Chen, P.-J.; Chung, C.-C.; Yaghoubi, A.; Liao, C.-N.; Diau, E. W.-G.; Chueh, Y.-L. Fabrication of Large-Scale Single-Crystal Bismuth Telluride (Bi_2Te_3) Nanosheet Arrays by a Single-Step Electrolysis Process. *Nanoscale* **2014**, *6*, 7780−7785.
(39) Hope, M. A.; Griffith, K. J.; Cui, B.; Gao, F.; Dutton, S. E.; Parkin, S. S. P.; Grey, C. P. The Role of Ionic Liquid Breakdown in the Electrochemical Metallization of VO_2: An NMR Study of Gating Mechanisms and VO_2 Reduction. *J. Am. Chem. Soc.* **2018**, *140*, 16685−16696.
(40) Si, C.; Choe, D.; Xie, W.; Wang, H.; Sun, Z.; Bang, J.; Zhang, S. Photoinduced Vacancy Ordering and Phase Transition in $MoTe_2$. *Nano Lett.* **2019**, *19*, 3612−3617.
(41) Leighton, C. Electrolyte-Based Ionic Control of Functional Oxides. *Nat. Mater.* **2019**, *18*, 13−18.
(42) Zhu, H.; Wang, Q.; Cheng, L.; Addou, R.; Kim, J.; Kim, M. J.; Wallace, R. M. Defects and Surface Structural Stability of $MoTe_2$ Under Vacuum Annealing. *ACS Nano* **2017**, *11*, 11005−11014.
(43) Rosenberger, M. R.; Chuang, H.-J.; McCreary, K. M.; Hanbicki, A. T.; Sivaram, S. V.; Jonker, B. T. Nano-"Squeegee" for the Creation of Clean 2D Material Interfaces. *ACS Appl. Mater. Interfaces* **2018**, *10*, 10379−10387.
(44) Chen, B.; Sahin, H.; Suslu, A.; Ding, L.; Bertoni, M. I.; Peeters, F. M.; Tongay, S. Environmental Changes in $MoTe_2$ Excitonic Dynamics by Defects-Activated Molecular Interaction. *ACS Nano* **2015**, *9*, 5326−5332.
(45) Kresse, G.; Hafner, J. *Ab Initio* Molecular Dynamics for Liquid Metals. *Phys. Rev. B: Condens. Matter Mater. Phys.* **1993**, *47*, 558−561.
(46) Kresse, G.; Hafner, J. *Ab Initio* Molecular-Dynamics Simulation of the Liquid-Metal–Amorphous-Semiconductor Transition in Germanium. *Phys. Rev. B: Condens. Matter Mater. Phys.* **1994**, *49*, 14251−14269.
(47) Kresse, G.; Furthmüller, J. Efficiency of *Ab-Initio* Total Energy Calculations for Metals and Semiconductors Using a Plane-Wave Basis Set. *Comput. Mater. Sci.* **1996**, *6*, 15−50.
(48) Kresse, G.; Furthmüller, J. Efficient Iterative Schemes for *Ab Initio* Total-Energy Calculations Using a Plane-Wave Basis Set. *Phys. Rev. B: Condens. Matter Mater. Phys.* **1996**, *54*, 11169−11186.
(49) Blöchl, P. E. Projector Augmented-Wave Method. *Phys. Rev. B: Condens. Matter Mater. Phys.* **1994**, *50*, 17953−17979.
(50) Kresse, G.; Joubert, D. From Ultra-Soft Pseudopotentials to the Projector Augmented-Wave Method. *Phys. Rev. B: Condens. Matter Mater. Phys.* **1999**, *59*, 1758−1775.
(51) Peng, H.; Yang, Z.-H.; Perdew, J. P.; Sun, J. Versatile van Der Waals Density Functional Based on a Meta-Generalized Gradient Approximation. *Phys. Rev. X* **2016**, *6*, 041005.
(52) Sun, J.; Ruzsinszky, A.; Perdew, J. P. Strongly Constrained and Appropriately Normed Semi-Local Density Functional. *Phys. Rev. Lett.* **2015**, *115*, 036402.
(53) Perdew, J. P.; Burke, K.; Ernzerhof, M. Generalized Gradient Approximation Made Simple. *Phys. Rev. Lett.* **1996**, *77*, 3865−3868.
(54) Togo, A.; Tanaka, I. First Principles Phonon Calculations in Materials Science. *Scr. Mater.* **2015**, *108*, 1−5.
(55) Zakhidov, D.; Rehn, D. A.; Reed, E. J.; Salleo, A. Reversible Electrochemical Phase Change in Monolayer to Bulk MoTe2 by Ionic Liquid Gating. 2019, *arXiv* (Materials Science), May 29, 2019, 1905.12746.https://arxiv.org/abs/1905.12746 (accessed February 6, 2020).

https://dx.doi.org/10.1021/acsnano.9b07095
ACS Nano XXXX, XXX, XXX−XXX